Soot characteristics from diffusion flames coupled with plasma

Dandan Qi[1,2], Yaoyao Ying[1,2], Danhua Mei[3], Xin Tu[4], Dong Liu[1,2,*]

[1] MIIT Key Laboratory of Thermal Control of Electronic Equipment, School of Energy and Power Engineering, Nanjing University of Science and Technology, Nanjing 210094, People's Republic of China.

[2] Advanced Combustion Laboratory, School of Energy and Power Engineering, Nanjing University of Science and Technology, Nanjing 210094, People's Republic of China.

[3] College of Electrical Engineering and Control Science, Nanjing Tech University, Nanjing, 211816, Jiangsu, China.

[4] Department of Electrical Engineering and Electronics, University of Liverpool, Liverpool L69 3GJ, UK.

---

[*] Corresponding author. E-mail: dongliu@njust.edu.cn (Dong Liu)

Abstract

The study of soot characteristics in plasma-flame interaction was necessary to improve combustion efficiency and reduce pollutant emissions. This work experimentally investigated effects of plasma on soot formation, evolution and characteristics in ethylene diffusion flames by both optical diagnostic and sampling methods. The optical diagnostic method was employed to capture the two-dimensional distribution of soot temperatures and concentrations. Moreover, the nanostructure, crystallite properties and oxidation reactivity of soot from diffusion flames with plasma addition were obtained using transmission electron microscopy, Raman spectroscopy, thermogravimetric analysis and X-ray diffraction spectroscopy. The flame shapes and luminosity varied depending on the electrical parameters and oxygen concentration.It was found that the overall temperature increased somewhat with plasma activation, but remained roughly constant when the discharge frequency or applied voltage increased. The soot concentration immediately reduced with plasma on and then displayed different trends as the discharge frequency or applied voltage increased. The variation in soot concentration was caused by the combination of several parameters, including flame behavior, soot temperature and the effect of the electric field by energetic and chemically active species. The generated soot showed typical chain-like aggregates without plasma, but more film-like materials were presented with plasma acting on flames. The soot graphitization degree decreased notably with plasma generation resulting in higher oxidation reactivity because the shorter residence time and the plasma activation were simultaneously obtained, which both illustrated an inhibition

effect of plasma on soot emissions. The disordered carbon content related to soot oxidation reactivity.

Keywords: Soot characteristics, Plasma, Diffusion flames

1. Introduction

Soot particles produced during the incomplete combustion of hydrocarbon fuels not only reduce the performance of the combustion system but also cause significant environmental pollution and health problems [1-3]. The increasing stringency of soot emission regulations has prompted a slew of studies investigating efficient combustion systems and devices. It is critical to take action to reduce soot emissions into the atmosphere. New insights into soot structure and oxidation reactivity enable us to better understand the soot production process and develop effective soot-reduction strategies. Nanoscale structural variations in soot have been found to affect its oxidation reactivity depending on fuel and combustion conditions [4-7]. Following that, numerous studies extensively investigated the correlation between soot internal structure and oxidation reactivity under different conditions [8-11] and established a strong structure property relationship.

Electric fields or plasma can be a viable option for combustion control. The influence of the external electric fields on the flames has been extensively investigated to develop advanced combustion systems with high energy efficiency to improve flame stability and reduce pollutant emissions. Calcote proposed an ionic mechanism based on two observations: the correlation between soot and charged species in the flame and the more rapid reactions between neutral species and charged hydrocarbon ions[56-58]. For soot formation, Calcote also pointed out the location of the ions just before the formation of soot nanoparticles and the similar soot and ionic concentrations [58]. In the electric field, the influence on soot inception is complicated by the production of an ionic wind. Weinberg et al. demonstrated that the soot growth is more or less associated with charged species and it can be controlled by an electric field [12]. The effects of flame exposure to an external electric field on soot emission have also been investigated in several experiments [13-16]. Park et al. [13] reported a less amount of soot particles in a counterflow non-premixed laminar flames using Direct Current (DC) electric fields. They found that the luminosity of the typical bright yellow flame caused by soot particles was reduced, indicating that the number of soot particles was reduced significantly by applying an electric field. Due to the heavy dependence of polycyclic aromatic hydrocarbons (PAHs) and soot formation on temperature, residence time, and fuel mole fraction [17], the modified flow field via the ionic wind may produce an unfavorable environment for soot formation and growth. Sayed-Kassem et al. [18] found that the soot volume fraction diminishes and the average primary particle diameter increased slightly in a diffusion flame when an electric field was applied. The main reason for this is that the ionic wind-driven flow field reduces the flow residence time and increases the temperature field, which are important factors for the formation and growth of soot. The accelerated chemical ions in the flame entrap air in such a way that the flame is aerated, increasing oxidation and thus reducing soot formation [59].

Plasma is a collection of neutral and charged particles which are electrically neutral on average and exhibit collective effects [19]. Compared to the thermal plasma, non-thermal plasma (NTP) has higher electron temperature and is more kinetically active due to the rapid production of active radicals and excited species via electron impact dissociation, excitation, and subsequent energy relaxation. On the one hand, the non-thermal plasmas generate high concentrations of cryogenic ions [21, 27, 28]. On the other hand, the efficient generation of radicals and active species allows plasma to change the kinetic pathway [19, 20]. Non-thermal plasma techniques have progressed in the field of soot emission suppression. Cha et al. [22] addressed the issue that the plasma could affect the soot formation process and combustion characteristics, while the temperature and the concentration of major species were not influenced much by the plasma generation. This conclusion was also verified in other investigations [23]. Non-thermal plasma has also been widely explored for soot emissions as an after-treatment method for engines. The challenge for conventional soot reduction methods is that they start working at a minimum temperature of 250 °C, while the typical exhaust temperatures of engines are in a wider range between 120 and 650 °C. In this temperature range, plasma is one of the most promising options for post-treatment technology. Okubo et al. [24] investigated the simultaneous treatment of soot and NO_x utilizing catalysis combined with non-thermal plasma. The soot was eliminated in their investigation under the condition of lean oxygen. Shi et al. [25] found the evolution law of deposited particles when a non-thermal plasma flowed through the diesel particulate filters. The weak component of the particle floc structure broke first during oxidation to form a chain structure.

Considering the exceptional performance of non-thermal plasma in reducing the formation and emission of soot particles, the aforementioned studies have extensively explored the corresponding variation of overall soot or the analysis of kinetics with regard to plasma addition. However, to our best knowledge, quite a few available studies have investigated the detailed influences of the plasma-flame interaction on soot emissions and characteristics in any systematic way. The study of soot characteristics in plasma-flame interaction was necessary to improve combustion efficiency and reduce pollutant emissions. It also helped to develop the relevant soot formation mechanisms in plasma-flame interaction and find a new way to remove the soot deposited in the combustion chamber. We aim to enhance the fundamental understanding of the soot characteristics in the plasma-flame interaction at ambient conditions by combining optical diagnostics of the diffusion flame and comprehensive characterization of the soot.

Based on the reasons above, the objective of this study is to investigate the effects of non-thermal plasma on the soot formation and combustion characteristics in hydrocarbon diffusion flames by adopting a wire-cylinder-type dielectric barrier discharge (DBD) reactor. In the current study, combinations of the optical and sampling methods were introduced to fully diagnose the soot characteristics. For the optical diagnostics, a two-color method was used to obtain the detailed two-dimensional temperature distributions and soot concentration under different experimental conditions. The soot shape was derived from transmission electron microscopy (TEM) image analysis after a thermophoretic sampling approach was utilized to sample soot particles inside the flame. A quartz plate sampling system was utilized to obtain soot particles in the flame exhaust for further soot reactivity research by thermogravimetric analysis (TGA), detailed crystallite analyses by X-ray diffraction (XRD), and Raman spectroscopy.

2. Experimental methodologies

2.1 Experimental setup and flame condition

Fig. 1 depicts the whole experimental system, which includes replaceable coflow burners, mass flow controllers (Sevenstar, CS200A), holders, mixing vessels, a nonthermal plasma-generating system, a visualization setup, a quartz glass plate with circulating water, and a thermophoretic sampling device. The burner featured an inner fuel nozzle made of a quartz tube with 4 mm i.d. and 6 mm o.d., as illustrated schematically in Fig. 1. The coflow oxidant was delivered through the outer tube, which had an 8 mm i.d. and a 10 mm o.d. The combustion in this tubular combustion chamber was isolated from the atmosphere because it took place inside the burner. Ethylene was selected as the base fuel because ethylene has been widely and extensively used for soot fundamental studies [7, 8, 13, 26]. Ethylene was not only an important fossil fuel but also an intermediate product of the pyrolysis of macromolecular hydrocarbon fuel. The fuel was ethylene (>99.95%), and the mixture of nitrogen and oxygen was used as an oxidizer. Mass-flow controllers were used for flow rate control with 98% accuracy.

The nonthermal plasma-generating system consisted of a DBD reactor, an electrical parameter monitoring system, and a power supply. The DBD reactor had a wire-cylinder-type electrode. In the center of the quartz tube, a stainless steel wire with an outer diameter of 1 mm served as an inner electrode and protruded 6 mm above the fuel nozzle exit. The wire protrusion was adopted to minimize excessive soot deposition and tip impacts on plasma formation. The cylindrical electrode made from a woven stainless mesh having a width of 4 mm surrounded the outer quartz tube, and it was located the 1 mm downstream from the fuel nozzle exit. The outer quartz tube served as a dielectric barrier for plasma generation to ensure the creation of a stable uniform plasma [21]. The DBD reactor was supplied by a high voltage pulse power supply with a peak-to-peak voltage of 20 kV and a frequency of 5 kHz. The applied voltage and current waveforms were measured by a high voltage probe (the Tektronix P6015A, bandwidth 75 MHz) and a current probe (Pearson 6585), respectively. All the electrical signals were sampled by a four-channel digital oscilloscope (TDS2024C). The sample rate of the oscilloscope is 2 GS/s. The combustion process was recorded using a digital single-lens reflex camera (Nikon Co. Ltd., D850, 24-85 mm lens) in front views to investigate the variation rules of flame morphologic characteristic parameters with plasma generation.

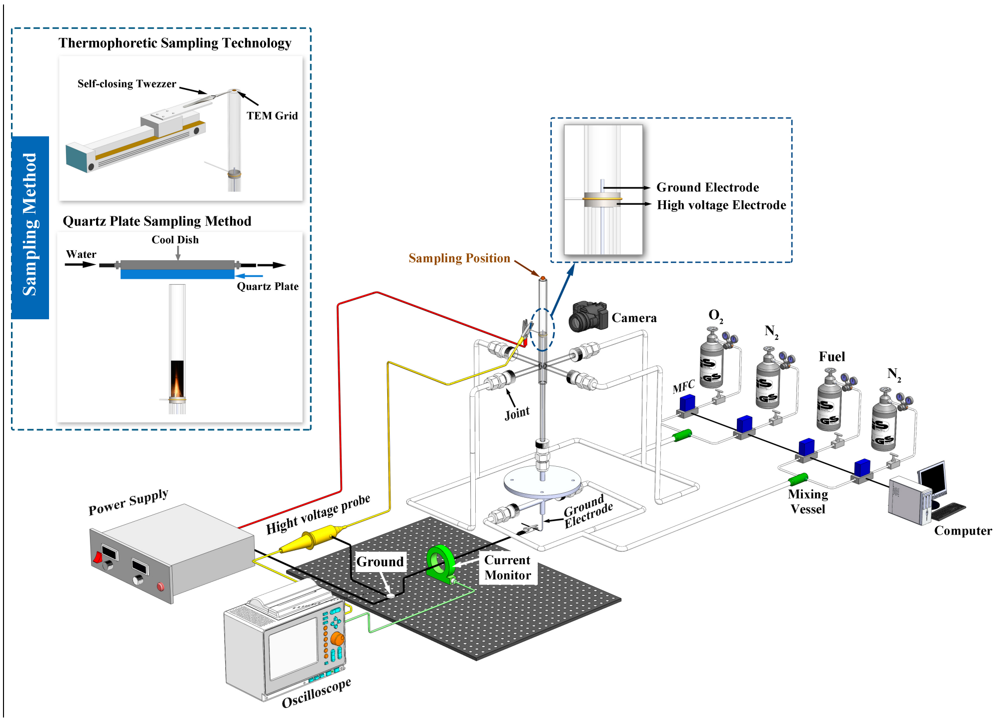

Fig. 1 Schematic diagram of experimental set up. (Color online)

The specific experimental flame conditions are listed in Table 1. For each condition, the fuel (ethylene) flow rate was fixed at 150 ml/min, and the total oxidant flow rate was fixed at 650 ml/min. To determine the effect of O_2 concentration and the plasma-flame interaction on soot formation and combustion characteristics, the O_2 concentration in the oxidant was increased from 21% to 40%, and the electrical parameters also varied for comparison. The O_2 concentration could not be further increased in the present study because the high temperature would damage the quartz combustor. Different flame notations could be found in Table 1.

Table 1. Flame experimental conditions.

Flame notation	Applied voltage, *U* (kV)	Discharge frequency, *f* (kHz)	O_2 concentration (X_O)	Gas flow rate (ml/min)			
				C_2H_4	N_2 (Diluent)	O_2	N_2 (Carrier)
21%-0-0	0	0	21%	150	100	136.5	513.5
21%-12-2.5	12	2.5					
21%-12-4.0	12	4.0					

21%-10-2.5	10	2.5					
21%-15-2.5	15	2.5					
25%-0-0	0	0	25%	150	100	162.5	487.5
25%-12-2.5	12	2.5					
25%-12-4.0	12	4.0					
25%-10-2.5	10	2.5					
25%-15-2.5	15	2.5					
30%-0-0	0	0	30%	150	100	195	455
30%-12-2.5	12	2.5					
30%-12-4.0	12	4.0					
30%-10-2.5	10	2.5					
30%-15-2.5	15	2.5					
35%-0-0	0	0	35%	150	100	227.5	422.5
35%-12-2.5	12	2.5					
35%-12-4.0	12	4.0					
35%-10-2.5	10	2.5					
35%-15-2.5	15	2.5					
40%-0-0	0	0	40%	150	100	260	390
40%-12-2.5	12	2.5					
40%-12-4.0	12	4.0					
40%-10-2.5	10	2.5					
40%-15-2.5	15	2.5					

2.2 Determination of two-dimensional distributions for temperatures and KL factors.

The optical diagnostic techniques were adopted to visualize the spatial distributions of temperature and soot. The system consists of an optical probe, a charge-coupled device (CCD) camera with the optical transmission, a frame grabber, a microcomputer, and associated software. The objective lens of the probe has a 90 viewing angle. The camera has a 1/3-inch CCD panel with a resolution of 960 H×1280 W pixels. A coupling lens with a focus of 25 mm portrays the flame onto the CCD panel. The frame grabber installed in the computer converts the analog image signal into digital images with 8-bit digitization. The entire imaging system provides a frame rate of 40 frames per second.

The two-color pyrometry method was adopted to measure the two-dimensional distributions of soot temperatures and *KL* factors since direct-contact temperature measurement of the flame inside the combustor using thermocouples was difficult and inconvenient. Two-color or multicolor approaches have been widely utilized to measure soot temperature and concentration in various combustion systems, and they have been proved useful and effective for flame and soot diagnosis [35-37]. The two-color pyrometry method can only measure the temperature of small substances (soot here) within a flame rather than its surrounding gas. But due to the tiny size of soot particles, the temperature difference between soot and the surrounding gas should be less than 10 K. Therefore, the temperature measured here by two-color method can be regarded as the flame temperature approximately. According to the examination results in our previous studies [52, 54, 55], the error of two-color method was less than 100 K or 5%, which met the accuracy of this work and was reasonable to conduct some comparisons based on the same standard. Based on the empirical correlation [39, 40], the *KL* factor can be used to qualitatively compare soot concentration (or soot volume fraction), with a greater value in a specific area indicating a higher soot concentration. More detailed principles and derivation process of the two-color pyrometry method are given in the previous studies [8, 52]. The wavelengths of red (700 nm) and green (546 nm) were chosen as the measurement temperature band in this experiment. In addition, for the presence of flame instability after the addition of plasma, at least five pictures are compared to establish the typicality and reproductivity of the results, respectively.

2.3 Soot characterizations

A quartz plate with circulating water was settled horizontally 1 mm upper the outlet of the channel to collect soot after successful ignition. The soot was then peeled off from the plate for further soot nanostructure and oxidation analyses. This sampling method was used for soot collection in many studies [5, 29, 53]. The collection duration was set at 10 min for the following characterization analyses in the present investigation because, in accordance with our earlier research [29, 30], it had little impact on the soot properties. Besides, a thermophoretic sampling device [5, 31], which was composed of an electric cylinder and a TEM grid fixed by a self-closing tweezer, was also used to capture soot at the outlet of the combustor (the same position of soot collection by quartz plate) for further TEM analysis.

In this study, the morphology evolution of soot samples was analyzed by a Philips Tecnai 12 transmission electron microscope. During this process, four or more different locations were selected to establish the typicality and accuracy of TEM results for each experimental condition. For quantitative information, several TEM images were processed using Nano Measurer software to evaluate the average sizes of soot particles with and without plasma activation.

Raman analysis can provide a measure of disorder relative to graphitic content and is based upon semi-empirical relationships for quantitative information. A Horiba Jobin-Yvon LabRAM HR800 confocal Raman microscope with a 10 mW Ar ion laser was used for the Raman spectroscopy analysis. The excitation wavelength is 514.5 nm. The laser power was decreased to ensure adequate repeatability of the spectra in order to avoid laser-induced heating effects on the change of the carbon structure. The Raman spectra were recorded in four different positions with an exposure time of 40 s in the range of 800-3500 cm^{-1}. The crystalline parameters of soot particles from various plasma-flame interactions were derived from XRD analysis. An X-ray powder diffractometer (Rigaku D/max 2500 PC) with Cu-Kα X-ray source ($\lambda = 0.154$ nm) was employed. XRD patterns were obtained at 45 kV and 100 mA in the 2θ range from 10° to 110° with a step size of $2\theta=0.02°$ and an angular speed of 1 s/step.

An STA 449 F3 Jupiter thermogravimetric analyzer from NETZSCH with recording software was used to evaluate the oxidation reactivity. Firstly, the soot sample with a load of 5±0.2 mg was uniformly placed into the crucible before the TGA test. The sample was then heated to 300 °C at a heating rate of 10 °C/min and held constant in the Ar atmosphere for 1 h to remove the volatile organic component (VOF). Finally, the soot sample was further heated to 500 °C, with 22% oxygen and 78% argon replacing the atmosphere at a total flow rate of 100 ml /min. The oxidation reactivity of each sample was evaluated by comparing the standardized mass loss curves of each soot during the isothermal process. In the thermogravimetric analysis experiment, three replications of the experiment under each condition were performed to establish the typicality and accuracy. According to our previous studies, the accuracy of this method was 95% with 4.7% uncertainty [30].

3. Results and discussion

3.1 Flame typical features

Fig. 2 depicts typical flame images under various experimental conditions. The photographs were arranged to increase oxygen content (21%-40%) from bottom to top, while the images from left to right displayed flames under various discharge settings.

The flame contained a weak yellow region at 21% O_2 concentration with small amounts of soot formation, but it got more yellow luminous at 30% and 40% O_2 atmospheres, suggesting a higher soot temperature and more soot generation. A possible reason for this discrepancy might be that the higher O_2 concentrations contributed to higher ethylene conversion rates and larger heat release, which accelerated the growth rate of the soot surface and resulted in more luminous areas detected from the soot radiation [31]. Furthermore, raising the O_2 concentration lessened the diluting impact by increasing the concentration of less inert N_2.

In this study, the cylindrical electrode was placed above the outflow of the burner inner tube to generate plasma in the flame region. Regardless of the effect of oxygen, Fig. 2 shows that the flame length and luminous intensity from the radiation of soot particles decreased rapidly when plasma was imposed on flames. The previous studies have reported that applying the high voltage electric field resulted in a decrease in flame length [22, 32]. The flame altered from roughly conical to nearly cylindrical. The flame length and light intensity dropped further as the discharge frequency increased, as seen in Fig 2. At varying oxygen concentrations, the flame height and light intensity showed different trends as the applied voltage rose. There may be three main reasons responsible for this phenomenon. First of all, the flame length of a diffusion flame is generally governed by the balance between the axial convection and the radial diffusion [32, 33]. In radial convection caused by ionic winds, the equilibrium mechanism can be changed. Radial convection might be important in strong streamers to reduce flame length. This effect is substantiated by the nearly cylindrical flame in the plasma regime.

In addition, plasma is well recognized for producing a large number of reactive species, including radicals such as O, O_3, OH, and H [34]. The effect of these reactive species produced by nonthermal plasma may also reduce flame length. The other factor is the reduced soot formation, which decreases the flame luminosity and also leads to a shorter path for soot particles before it was oxidized out of the flame reaction zone.

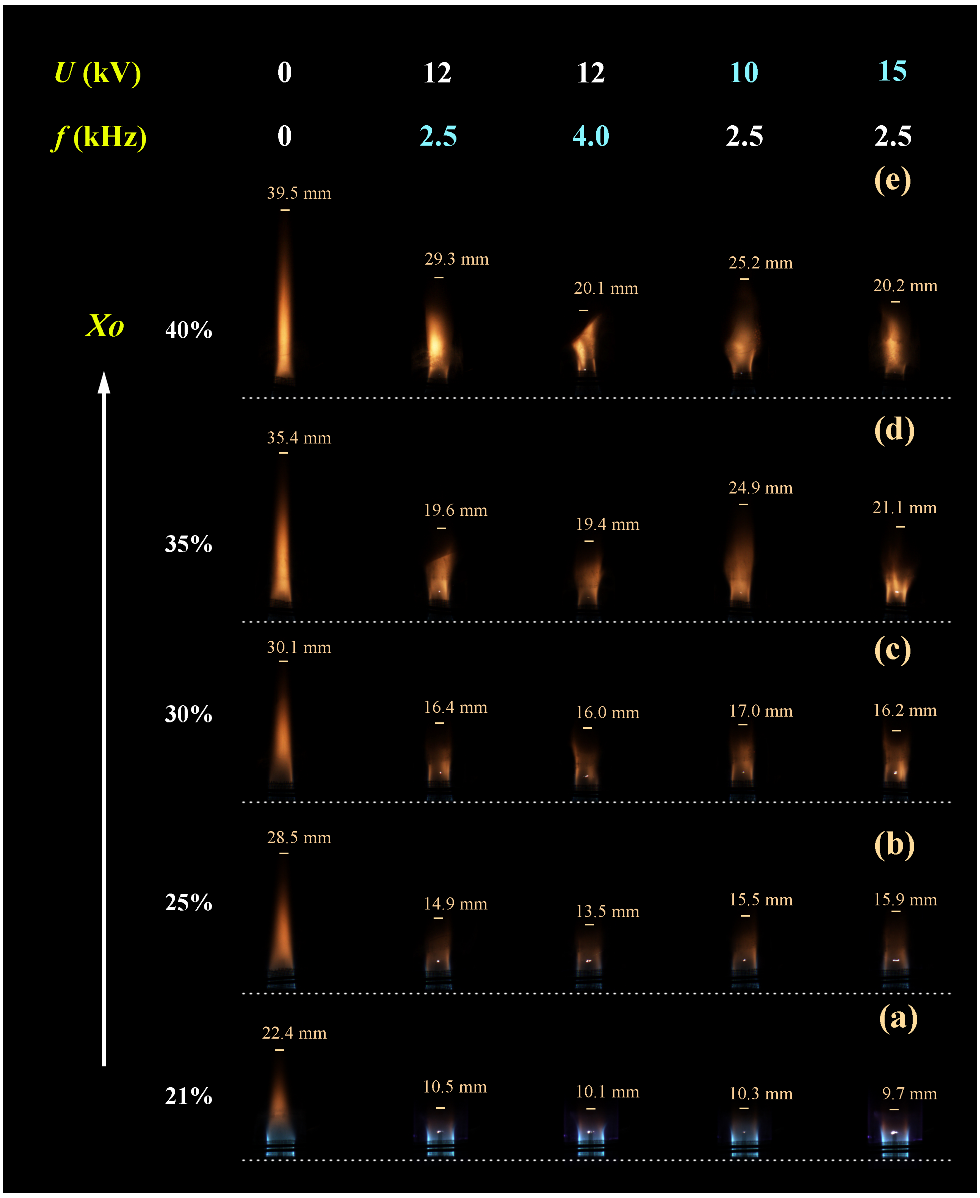

Fig. 2 Representative images of flames at various conditions, (a) $X_O = 21\%$, (b) $X_O = 25\%$, (c) $X_O = 30\%$, (d) $X_O = 35\%$, (e) $X_O = 40\%$. (Color online)

3.2 Temperature and KL factor distributions

The measured distributions of soot temperatures with different oxygen concentrations at various plasma discharge conditions are presented in Fig. 3, with the mean temperature and the peak temperature marked above each image, respectively. The maximum temperature (T_{max}) remained constant approximately at the same oxygen concentration. In the case of pure flame, the mean temperature (T_{mean}) of the flame grew dramatically as oxygen content increased. It could be explained that higher temperatures were discovered as the oxygen concentration increased, owing to the participation of more fuel and a greater amount of heat release amount. With plasma generation, there was a slight tendency for the mean temperature to rise at all oxygen concentrations. The mean temperature fluctuated within 5 K with the increase of the applied voltage and discharge frequency. The temperature difference with the variation of electrical parameters has been discovered to be insignificant. In addition, the distribution of soot temperatures had altered significantly compared with that without the presence of plasma. It could be observed from Fig. 3 that although the flame height decreased and the low-temperature zone decreased with plasma generation, the high-temperature zone expanded.

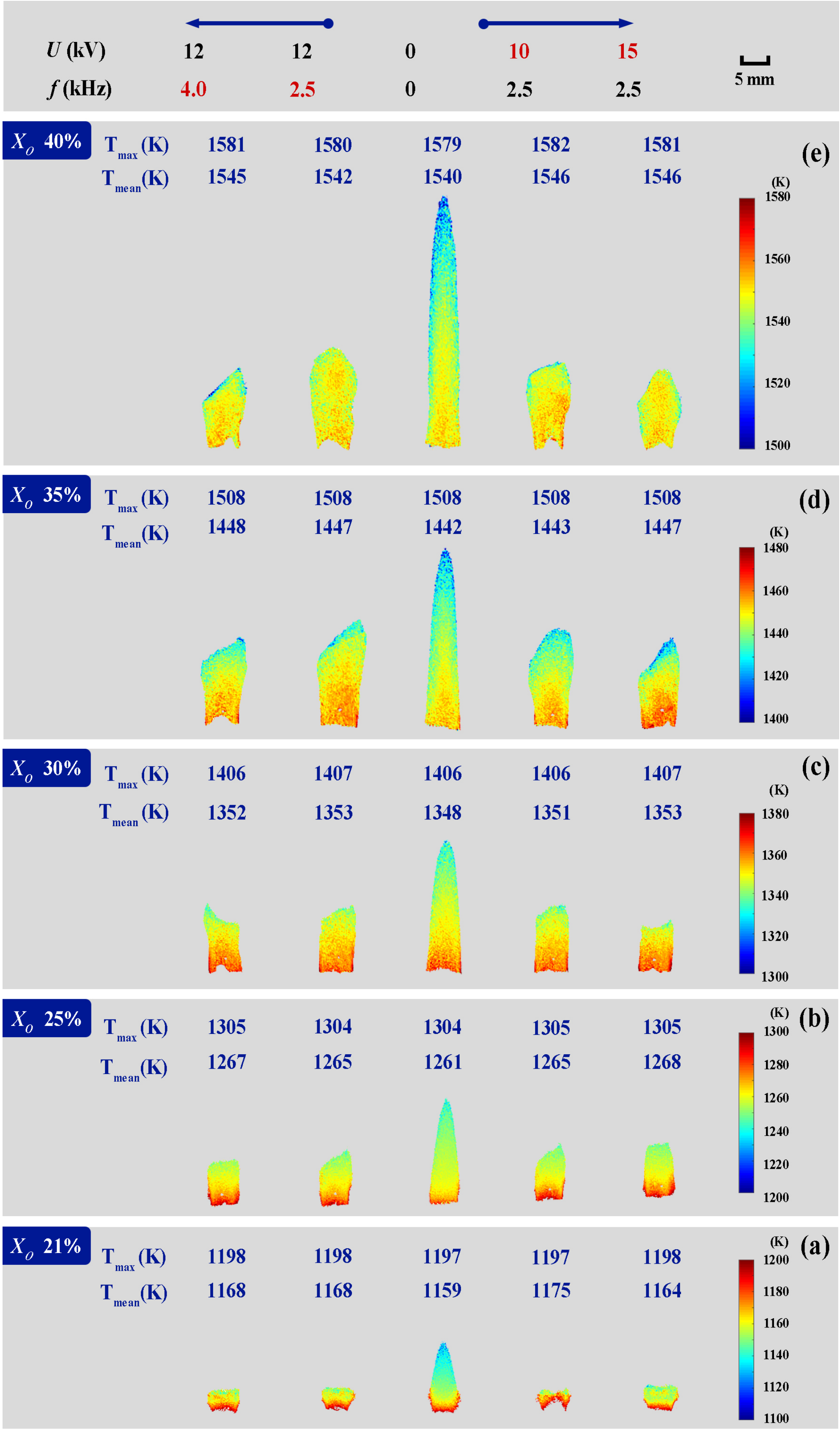

Fig. 3 Temperature distributions for the variation of discharge conditions at different oxygen concentration combustion conditions, (a) $X_O = 21\%$, (b) $X_O = 25\%$, (c) $X_O = 30\%$, (d) $X_O = 35\%$, (e)

X_O = 40%. (Color online)

The distributions of *KL* factors at different oxygen concentrations at various plasma discharge conditions were presented in Fig. 4, and the mean *KL* factor (KL_{mean}) was marked above each image, respectively. The *KL* factor could be used to compare the soot concentration (or soot volume fraction) qualitatively, with a greater value indicating higher soot concentration in that region [38, 41]. Without the presence of plasma, KL_{mean} grew dramatically as oxygen concentration increased. In Fig. 4, the overall soot concentration decreased rapidly at first with plasma generation and then further revealed different tendencies as the higher discharge frequency or higher applied voltage was induced. As the discharge frequency increased, the soot concentration decreased regardless of oxygen concentration. This tendency was well consistent with the results from planar laser-induced incandescence (PLII) and fluorescence (PLIF) techniques by Park et al. [13] as well as the previous section's visual observation of flame luminosity in Fig. 2. When the voltage was 10 kV, it could be found that the *KL* factors were significantly lower than when there without plasma, such as from 0.0845 to 0.0229 (X_O = 21%), from 0.1241 to 0.0538 (X_O = 25%), from 0.1468 to 0.0998 (X_O = 30%), from 0.1786 to 0.1167 (X_O = 35%), from 0.2029 to 0.1864 (X_O = 40%). However, as the applied voltage increased from 10 kV to 15 kV, the alteration in soot concentration did not reflect an obvious regularity. Soot suppression performance cannot be determined just by considering voltage variation alone. The soot concentration can be affected by several factors simultaneously with the nonthermal plasma. Firstly, the number of discharge channels generated per unit time increases as the discharge frequency enhances. The collision probability of high-energy electrons and particles in the flame increased accordingly, which might promote the reduction of soot concentration. According to Matsuzawa et al. [16], plasma-induced reaction intensification could help convert ionic species into neutral non-soot-precursors and reduce soot precursor emissions. The electric field intensity increased as the applied voltage increased at a constant discharge frequency. In a single discharge cycle, more gas breakdowns occurred, which meant that the number and average energy of electrons significantly increased. The intensified reaction between electrons and gas resulted in the production of more active species [42], which promoted the oxidation of soot. Song et al reported the abatement capability of particulate matter (PM), hydrocarbons (HCs), and NO_x from an actual diesel exhaust as functions of voltage at a fixed frequency [43]. Secondly, in the case of the same flow rate of fuel and oxidizer, the alteration of flame length affects the residence time of soot growth, which affects the soot concentration in the flame. The modified flow field through the ionic wind may provide an unfavorable environment for soot to form and grow, because the formation of PAHs and soot particles depends on temperature, residence time in a hot environment, and fuel mole fraction [13, 17]. Finally, soot temperatures may have an impact on the soot inception and surface growth rate as well. Therefore, when the plasma interacts with the flame directly, the synergy of the above three factors influenced the soot concentration.

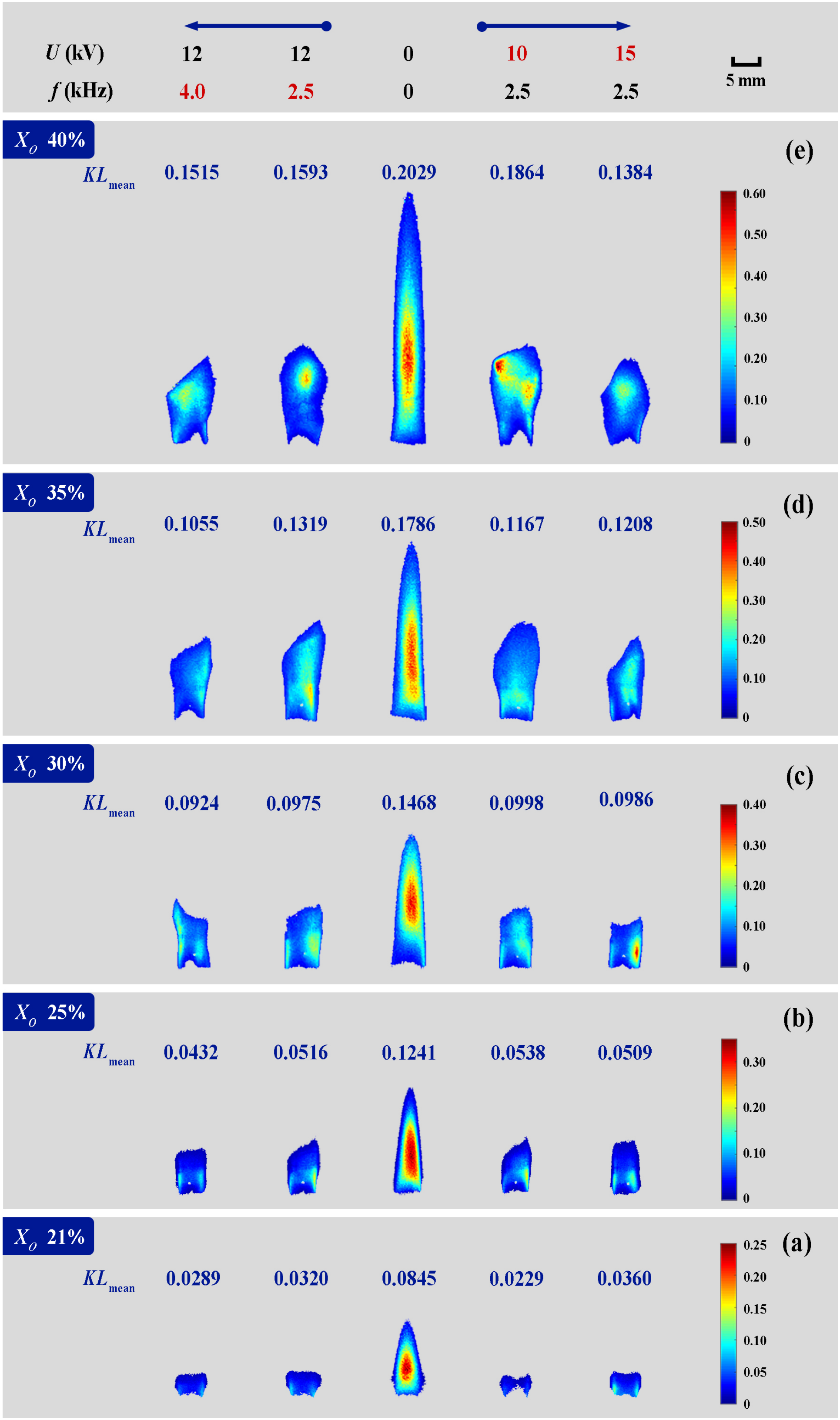

Fig. 4 *KL* factor distributions for the variation of discharge conditions at different oxygen concentration combustion conditions, (a) $X_O = 21\%$, (b) $X_O = 25\%$, (c) $X_O = 30\%$, (d) $X_O = 35\%$, (e)

X_O = 40%. (Color online)

3.3 Soot morphology evolutions

Representative TEM morphological images of the soot samples with and without plasma discharge are illustrated in Fig. 5 with a resolution of 100 nm. The soot morphology without plasma appeared to be chain-like or tufted aggregates composed of hundreds of monomers or spherules with legible margins, as indicated by the white arrows. Many prior investigations [44, 45] had reported morphology of mature soot that looked similar to this structure. They were a resemblance to the particle collision and agglomeration process, which implied the high maturity of soot [9, 12]. The TEM results clearly showed the different characteristics of soot. However, in the case of plasma activation, the evolution of soot morphology started to happen. Some larger films or liquid-like materials with less defined boundaries and irregular-shaped protrusions appeared, as marked by the yellow arrows. At the higher oxygen concentrations ($X_O \geq 35\%$), more liquid-like materials could be observed, and the chain structure was still visible as the discharge frequency increased. When the plasma with higher frequency was introduced to flames with a lower oxygen concentration ($X_O <$ 35%), the morphology of soot particles exhibited typical film-like materials with hardly visible chain-like clusters of small particles. These could be attributed to the chemical condensation of heavy PAHs, indicating an early stage of the soot production process [7, 46]. However, the evolution of soot morphology did not follow a monotonous regularity with the increase of applied voltage. This phenomenon was presumably caused by the cooperation of multiple factors, such as the residence time variation, the different temperatures, and a direct effect of plasma via activation of species. These observations well illustrated the morphology evolutions in the suppression process of soot formation with various plasma discharges.

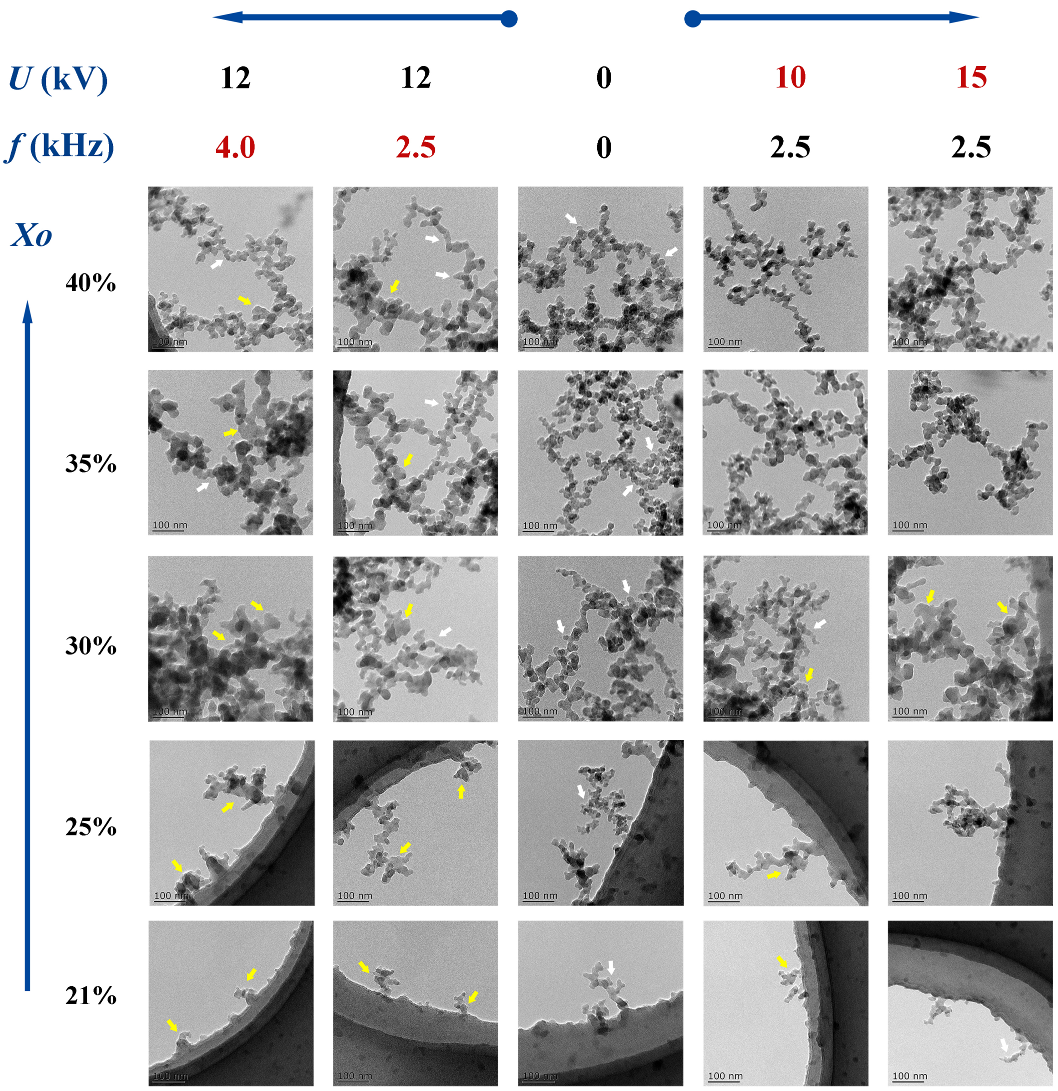

Fig. 5 Morphology transition of soot (length scale of 100 nm) with various plasma discharge conditions. (Color online)

The primary particle diameters were calculated using Nano Measurer particle size statistics software, which captured images for statistics at each location. Since there the number of soot particles collected at low concentrations ($X_O < 30\%$) was limited, only the primary particle sizes at higher oxygen concentrations ($X_O \geq 30\%$) were given here for comparison. Fig. 6 depicts the mean primary particle diameter (d_p) in flames with various plasma discharge conditions. In general, d_p gradually decreased with oxygen concentration. d_p decreased rapidly due to the soot oxidation with the oxygen concentration ranging from Xo = 30% to 40% [47]. Another intriguing aspect of the soot collected through plasma-flame interaction was that the soot particle size is larger than that from the flame without plasma discharge. Moreover, as the discharge frequency increased, a larger d_p could be obtained. In fact, on the one hand, it might be because the particles are bigger and more nascent containing film-like particles. Matsuzawa et al. argued that the plasma-induced reaction intensification may aid in the conversion of ionic species into neutral non-soot precursors [16]. On the other hand, the flame with plasma discharge is distinctly shorter than without plasma, which reduces the oxidation process in combustion. Thus, the degree of soot oxidation with plasma activation reduces, which results in larger particle size. The effect of increasing applied voltage on soot particle size has no discernible trend due to the synergistic influence of many factors. Three major factors might be responsible for the difference in the d_p, including (1) the flame behavior, which might affect the residence time of soot particles in flames; (2) soot temperature, which might affect the soot inception and surface growth rates (3) a direct effect of electric field via activation of species.

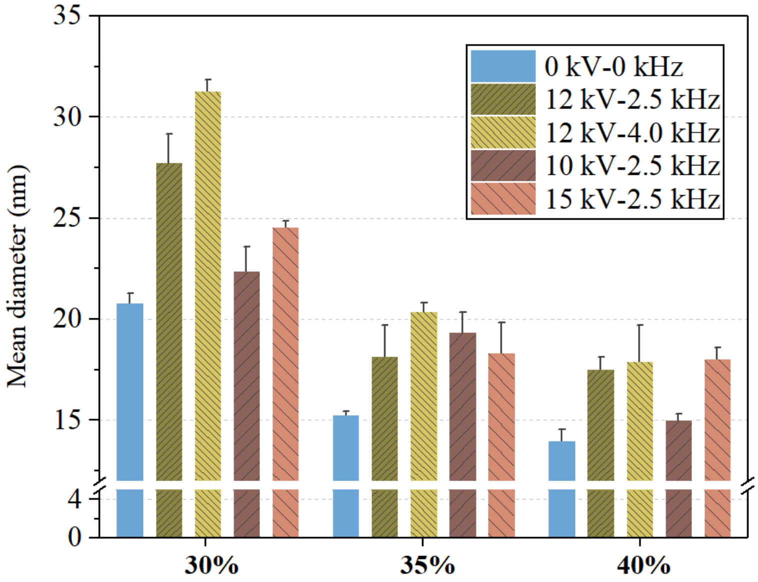

Fig. 6 Mean diameter of soot particles. (Color online)

3.4 Raman spectra analysis

Some mass Raman spectrum, XRD patterns and loss curves of the low oxygen concentration (*Xo* = 21%, 25%, 30%) were missing because the soot production under these conditions was quite small and it was difficult to collect enough quality for further analysis. Therefore, we chose two oxygen concentrations (*Xo* = 35% and *Xo* = 40%) for further analysis of the soot characteristics, including Raman spectra, XRD, and TGA analysis. Fig. 7 shows the Raman spectra of soot samples along with curve fittings for identifying the first-order spectral parameter. The Raman spectra were analyzed with a five-band curve fitting method as in previous studies done [5, 29, 48]. Four Lorentzian functions (for the graphite band G at ~1580 cm^{-1}, and the defect bands D1, D2, and D4 at ~1350 cm^{-1}, 1620 cm^{-1} and 1180 cm^{-1}, respectively) and one Gaussian function (for the defect band D3 at ~1500 cm^{-1}) were used. The G-peak and the D2-peak designated for the soot samples could move within a narrow range around 1580 cm^{-1} and 1620 cm^{-1} to have a good fit for the curve. All signals were normalized to the peak intensity. Data on the first-order band locations (Raman Shift), full width at half maximum (FWHM), and integrated intensity ratios of D1 and G bands (I_D/I_G) of soot samples are presented in Tables S1 and S2. The mean values of the G band FWHM measured for soot without plasma activation were 73 cm^{-1} for Xo = 35% and 71 cm^{-1} for Xo = 40%. Higher values were observed for the soot at the plasma-flame interaction: 77 cm^{-1} and 74 cm^{-1}. The D1 bands FWHM for the soot without plasma were slightly lower (172 cm^{-1}) than for all the investigated soot with plasma (185-188 cm^{-1}) for Xo = 35%, indicating that the wider crystallite size distributions in soot samples with plasma activation [29]. The mean values of the FWHM for the D3 band with plasma varied in the range of 97-104 cm^{-1} for Xo = 35%, which was larger than that of the soot (90 cm^{-1}) from the flame without plasma discharge. The higher values of the FWHM for the D3 band with plasma activation indicated more amorphous carbon content. For the distinction of the different soot samples, the D4 band FWHM showed no tendency for changes with the conditioning.

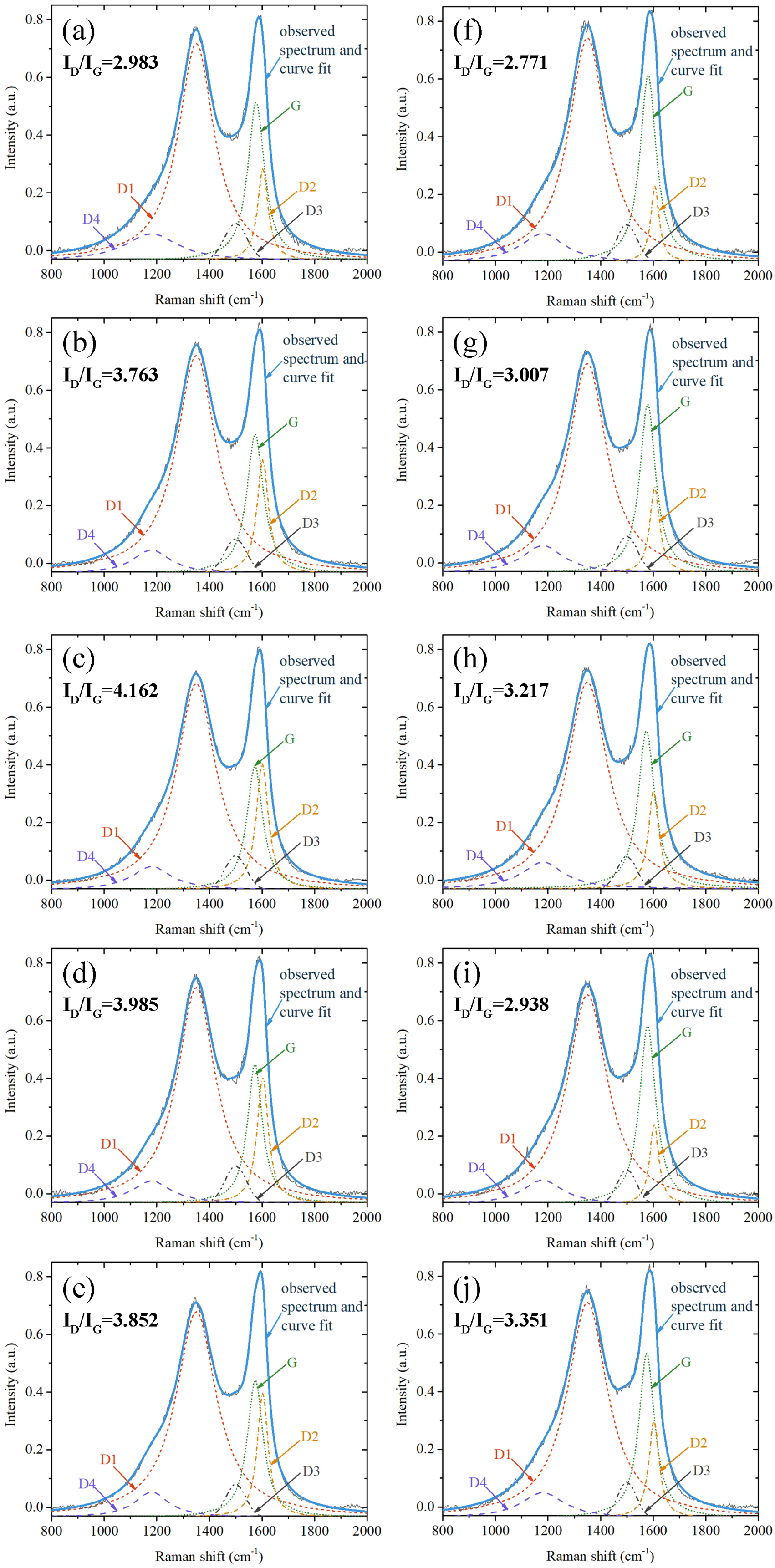

Fig. 7 Curve fit with band combination for the first-order Raman spectra of soot particles collected

from the flame conditions with various plasma discharges: (a) 35%-0-0, (b) 35%-12-2.5, (c) 35%-12-4.0, (d) 35%-10-2.5, (e) 35%-15-2.5, (f) 40%-0-0, (g) 40%-12-2.5, (h) 40%-12-4.0, (i) 40%-10-2.5, (j) 40%-15-2.5. (Color online)

The I_D/I_G ratio is commonly used to assess the degree of disorder in soot by comparing the integrated intensity of the D1 band with the fitted G band, as shown in Fig. 8. For Xo =35%, the I_D/I_G ratios of soot from different flames exhibited a ranking of 35%-0-0 (2.983 ± 0.281) < 35%-12-2.5 (3.763 ± 0.280) < 35%-15-2.5 (3.852 ± 0.309) <35%-10-2.5 (3.985 ± 0.248) <35%-12-4.0 (4.162 ± 0.228). The result illustrated the soot with plasma activation was more disordered. The soot samples with plasma at the higher discharge frequency contained more disordered carbon. The same pattern regarding the plasma's impact on soot for Xo = 35% was also seen in Xo = 40% cases. However, the I_D/I_G showed no tendency for changes with the applied voltages, which might be associated with the synergistic influence of many factors such as the flame length, soot temperature, and a direct effect of plasma via activation of species. The results in this chapter indicated that the I_D/I_G ratios of soot with plasma discharge were higher than those of soot without plasma, implying that the soot with plasma is more disordered and has a lower degree of graphitization. Since disordered carbon is more vulnerable to oxygen attack [49, 50], soot from flames with plasma may be more reactive.

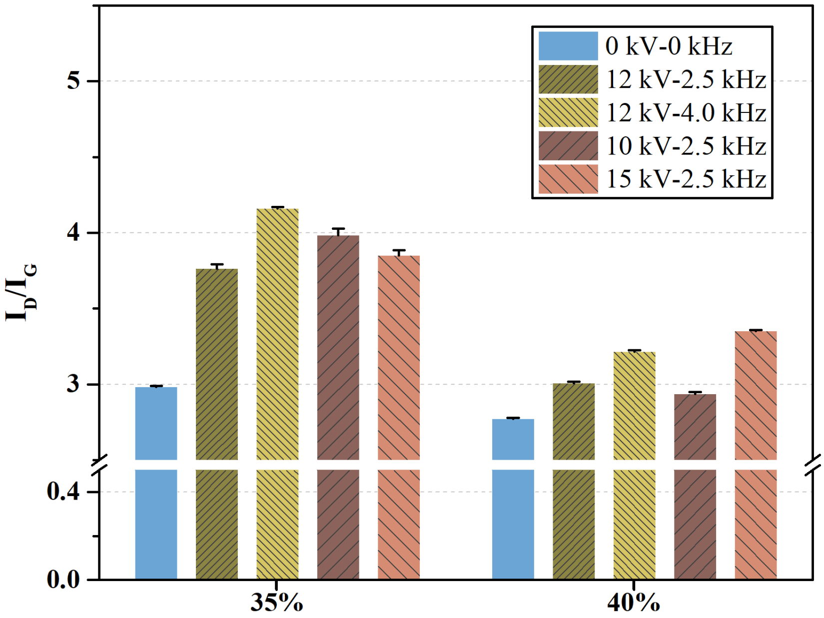

Fig. 8 I_D/I_G ratios for soot samples derived from different flames. (Color online)

3.5 XRD analyses for soot

Fig. 9 illustrates the baseline corrected diffraction patterns of soot from the post-flame region with plasma. A distinct primary peak at ~24° is observed in all patterns, which was 002 reflection. The 002 reflections indicate the presence of crystalline graphite carbon, and their asymmetrical characteristics show that PAHs contain aliphatic chains [51]. As shown in Fig. 10, the peak diffraction angles of soot particles under different conditions were extracted from the XRD spectra in Fig. 9. The soot diffraction peak shifted to the right for conditions of increasing oxygen concentration (35%-0-0, 40%-0-0) suggesting that the increase in oxygen concentration caused the higher soot graphitization degree. This result further verified the Raman observation of the higher soot graphitization degree as the oxygen concentration increased. Moreover, with plasma generation, the soot diffraction peak shifted left visibly. The result suggested that soot with plasma activation was less graphitic and more reactive. For the conditions of an increasing discharge frequency (35%-12-2.5, 35%-12-4.0, 40%-12-2.5, and 40%-12-4.0), the soot diffraction peak shifted left all the time, which represented the decline of the soot graphitization degree. However, as the applied voltage increased (35%-10-2.5 and 35%-15-4.0), the soot diffraction peak first shifted left and then right slightly for *Xo* = 35%, indicating the soot graphitization degree decreased first and then increased. When the applied voltage was increased with a fixed discharge frequency (40%-10-2.5 and 40%-15-4.0), the soot diffraction peak still shifts left all time. The results above from the XRD measurement show a good agreement with the result obtained from the Raman analysis.

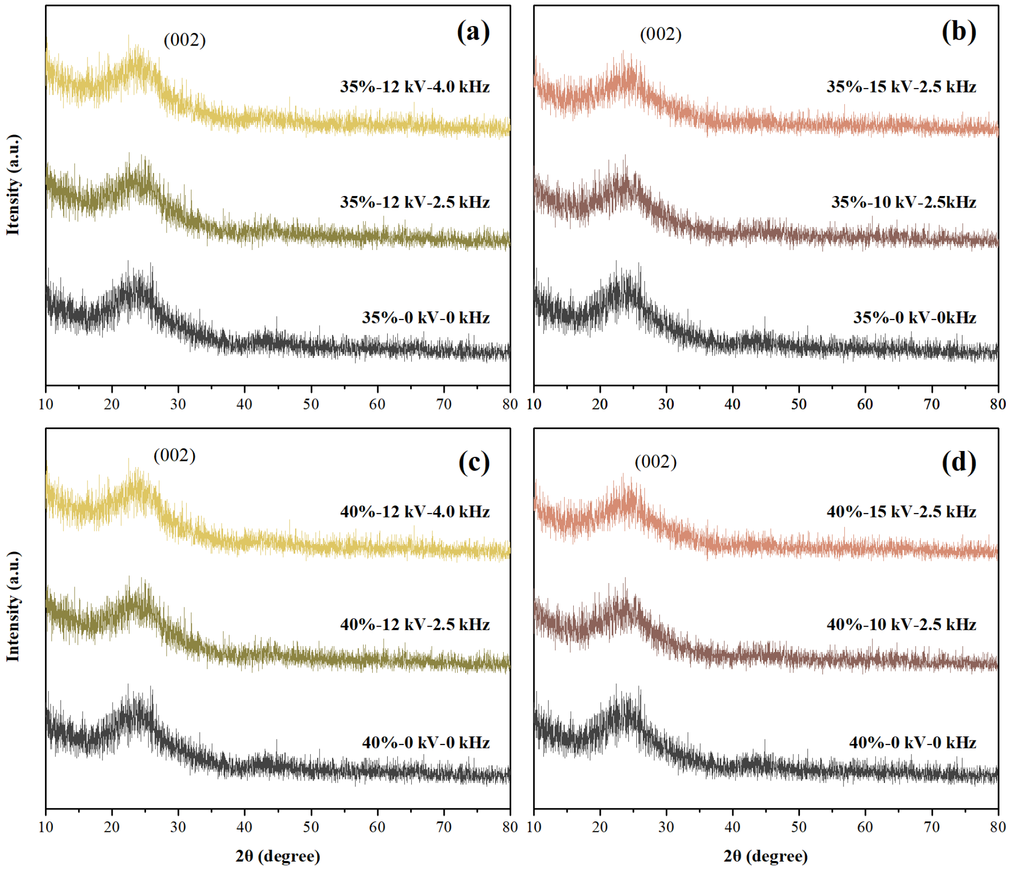

Fig. 9 XRD patterns of soot particles under different flame conditions: (a-b) X_O=35%, (c-d) X_O=40%. (Color online)

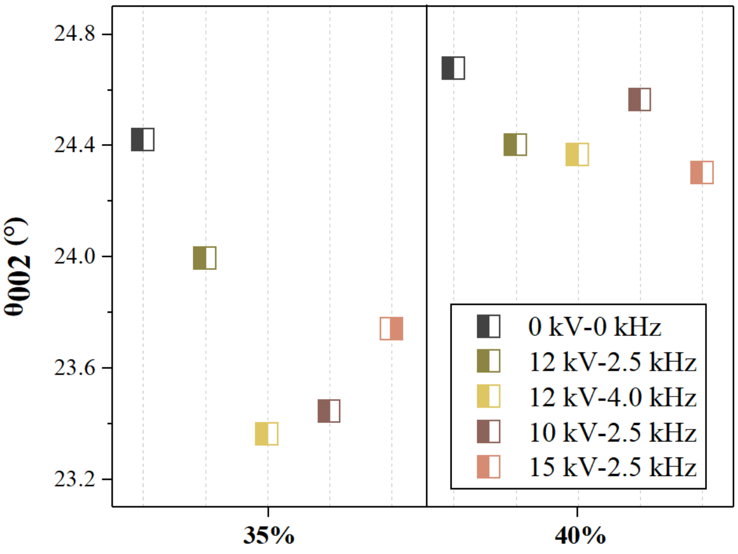

Fig. 10 The peak diffraction angles of soot particles under different conditions. (Color online)

3.6 Isothermal oxidation of soot

Fig. 11 illustrates the results of soot oxidation reactivity, which reflected the chemical properties of soot under various conditions to some extent. The normalized weight curves show an oxidation reactivity order of soot from flames. The overall mass loss curves displayed a similar trend but distinct oxidation rates. The larger slope of the mass loss curve meant a higher oxidation rate of soot and represented stronger reactivity.

As illustrated in Fig. 11, soot with a higher oxidation rate was detected in the higher oxygen concentration without plasma generation. Furthermore, regardless of the oxygen concentration, soot produced from the plasma-flame interaction had a stronger reactivity than it from the flames without plasma. This variation in soot oxidation behavior depended on their nanostructure differences. As shown in section 3.3, soot from the plasma-flame interaction presented a film-like material with irregular shaped protrusions. This kind of structure evolved from the chemical condensation of heavy PAHs, indicating that the soot was still young. It had been demonstrated in Section 3.4

that more disordered carbon was observed in the nanostructure of soot produced from the plasma-flame interaction. Since disordered carbon is more vulnerable to oxygen attack [49, 50], soot from flames with plasma may be more reactive. TGA results further confirmed that plasma generation could indeed enhance soot oxidation reactivity since the soot has a low carbonization degree with more disordered carbon. In Fig. 11, regardless of oxygen concentration, soot from the plasma-flame interaction with the higher discharge frequency (35%-12-4.0 and 40%-12-4.0) always exhibited a stronger reactivity than that produced with the lower discharge frequency (35%-12-2.5 and 40%-12-2.5) for the same applied voltage, which also had reasonable consistency with the analyses of TEM and Raman data that the plasma-flame interaction contributed to the formation of soot with lower carbonization degree. However, the enhancement of the applied voltage (from 10 kV to 15 kV) induced the decreased reactivity of the soot samples at Xo = 35%. The soot reactivity increased as the applied voltage was increased with fixed discharge frequency (40%-10-2.5 and 40%-15-4.0) for Xo = 40%. The plasma activation, a shorter residence time, and temperature variation contributed to the formation of soot with different levels of carbonization and reactivity. In conclusion, the different characteristics of soot were further confirmed by TGA results.

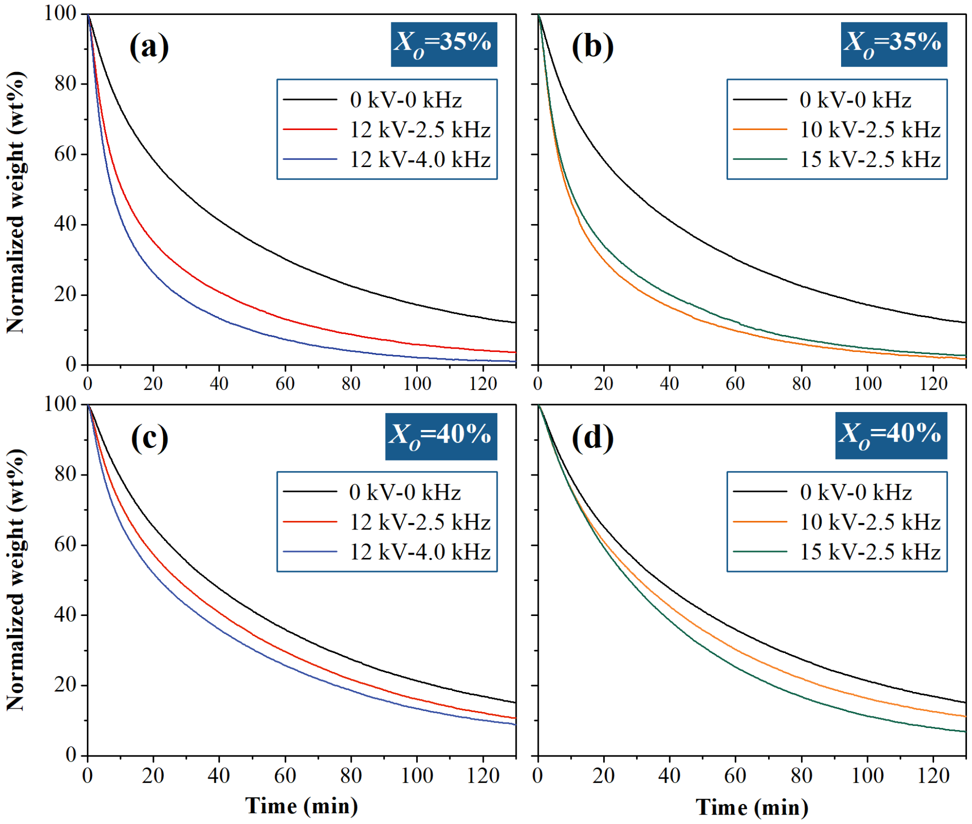

Fig. 11 TGA curves of soot particles for the various discharge conditions in both O_2 concentration: (a-b) X_O=35%, (c-d) X_O=40%. (Color online)

4. Conclusion

The present work was designed to understand the effects of plasma-flame interaction on the combustion characteristics and the evolutions of soot morphology, graphitization degree, and reactivity in diffusion flames by using optical diagnostic and sampling methods. The flame shapes and luminosity varied depending on the electrical parameters and oxygen concentration. The flame length was decreased as the plasma was coupled to the flame, which might be attributed to the increase of radial convection induced by ionic wind. The overall soot concentration decreased rapidly at first with plasma generation and then further revealed different tendencies as the higher discharge frequency or higher applied voltage was induced. The variation of the soot concentration across the flame depended on a variety of factors, including flame behavior, soot temperature, and the effect of energetic and chemically active species. The alteration of flame length affects the residence time of soot growth, which affects the soot concentration in the flame. Considering that the variation of soot temperature might affect the soot inception and surface growth rates, the slight increase in temperature could advance the generation of soot with the plasma-flame interaction. The intensified reaction between electrons and gas resulted in the production of more active species, which promoted the oxidation of soot. The generated soot showed typical chain-like aggregates without plasma activation, but more film-like materials were presented as plasma was turned on. The soot graphitization degree decreased notably with plasma generation because the shorter residence time and the plasma activation were simultaneously obtained, which both illustrated an inhibition effect of plasma on soot emissions. The soot reactivity with plasma activation was higher than that of the soot without plasma because soot produced by the plasma-flame interaction had more disordered carbon which was more accessible to oxygen. The plasma activation, flame length alteration, and temperature variation all contributed to the soot with different carbonization degrees and reactivity.

Acknowledgments

This work was supported by the National Natural Science Foundation of China [52076110, 52106160, 51822605], Jiangsu Provincial Natural Science Foundation of China [BK20200490], the Fundamental Research Funds for the Central Universities [30920031103].

References

[1] McEnally CS, Pfefferle LD, Atakan B, Kohse-Höinghaus K. Studies of aromatic hydrocarbon formation mechanisms in flames: Progress towards closing the fuel gap. Prog Energy Combust Sci 2006;32:247–94.

[2] Fiorito S, Mastrofrancesco A, Cardinali G, Rosato E, Salsano F, Su DS, et al. Effects of carbonaceous nanoparticles from low-emission and older diesel engines on human skin cells. Carbon 2011;49:5038–48.

[3] Maione M, Fowler D, Monks PS, Reis S, Rudich Y, Williams ML, et al. Air quality and climate change: designing new win-win policies for Europe. Environ Sci Policy 2016;65:48–57.

[4] Vander Wal RL, Tomasek AJ. Soot oxidation: Dependence upon initial nanostructure. Combust Flame 2003;134:1–9.

[5] Ying Y, Liu D. Nanostructure evolution and reactivity of nascent soot from inverse diffusion flames in CO_2, N_2, and He atmospheres. Carbon 2018;139:172–80.

[6] Chu H, Ya Y, Nie X, Qiao F, E J. Effects of adding cyclohexane, n-hexane, ethanol, and 2,5-dimethylfuran to fuel on soot formation in laminar coflow n-heptane/iso-octane diffusion flame. Combust Flame 2021;225:120–35.

[7] Li Q, Song C, Yan Z, Cao X, Wang J, Huang Z. Effects of $NH_3/H_2/N_2$ addition on soot morphology and nanostructure in laminar co-flow ethylene diffusion flame. Int J Hydrogen Energy 2022;47:16321–34.

[8] Chen M, Liu D. Morphology and nanostructure transitions of soot with various

dimethyl ether additions in nonpremixed ethylene flames at different scales. Energy Fuels 2020;34:16705–19.

[9] Ghiassi H, Toth P, Jaramillo IC, Lighty JAS. Soot oxidation-induced fragmentation: Part 1: The relationship between soot nanostructure and oxidation-induced fragmentation. Combust Flame 2016;163:179–87.

[10] Mahmoud NM, Yan F, Zhou M, Xu L, Wang Y. Coupled effects of carbon dioxide and water vapor addition on soot formation in ethylene diffusion flames. Energy Fuels 2019;33:5582–96.

[11] Apicella B, Pré P, Alfè M, Ciajolo A, Gargiulo V, Russo C, et al. Soot nanostructure evolution in premixed flames by High Resolution Electron Transmission Microscopy (HRTEM). Proc Combust Inst 2015;35:1895–902.

[12] Manyo P, Weinberg F. On the size, charge and number-rate of formation of carbon particles in flames subjected to electric fields. Proc R Soc Lond A Math Phys Sci 1970;319:351–71.

[13] Park DG, Choi BC, Cha MS, Chung SH. Soot reduction under DC electric fields in counterflow non-premixed laminar ethylene flames. Combust Sci Technol 2014;186:644–56.

[14] Xie L, Kishi T, Kono M. Investigation on the effect of electric fields on soot formation and flame structure of diffusion flames. Symp Combust 1992;24:1059–66.

[15] Liu A, Luo KH, Rigopoulos S, Jones W. Effects of the electric field on soot formation in combustion: A coupled charged particle PBE-CFD framework.

Combust Flame 2021:111796.

[16] Matsuzawa Y, Suzuki J, Horisawa H, Kimura I. Effect of electron injection for soot suppression in hydrocarbon flames. Vacuum 2013;88:79–82.

[17] Joo PH, Wang Y, Raj A, Chung SH. Sooting limit in counterflow diffusion flames of ethylene/propane fuels and implication to threshold soot index. Proc Combust Inst 2013;34:1803–9.

[18] Sayed-Kassem A, Gillon P, Idir M, Gilard V. On the effect of a DC electric field on soot Pparticles' emission of a laminar diffusion flame. Combust Sci Technol 2022;194:213–24.

[19] Ding W, Xia M, Shen C, Wang Y, Zhang Z, Tu X, et al. Enhanced CO_2 conversion by frosted dielectric surface with ZrO_2 coating in a dielectric barrier discharge reactor. J CO_2 Util 2022;61:102045.

[20] Wang Y, Yang W, Xu S, Zhao S, Chen G, Weidenka A, et al. Shielding Protection by Mesoporous Catalysts for Improving Plasma-Catalytic Ambient Ammonia Synthesis. J Am Chem Soc 2022;144:12020-31.

[21] Lu X, Laroussi M, Puech V. On atmospheric-pressure non-equilibrium plasma jets and plasma bullets. Plasma Sources Sci Technol 2012;21:034005.

[22] Cha MS, Lee SM, Kim KT, Chung SH. Soot suppression by nonthermal plasma in coflow jet diffusion flames using a dielectric barrier discharge. Combust Flame 2005;141:438–47.

[23] Tamadonfar P, Gülder ÖL. Effect of burner diameter on the burning velocity of premixed turbulent flames stabilized on Bunsen-type burners. Exp Therm Fluid

Sci 2016;73:42–8.

[24] Okubo M, Yamada H, Yoshida K, Kuroki T. Simultaneous reduction of diesel particulate and NO_x using a catalysis-combined nonthermal plasma reactor. IEEE Trans Ind Appl 2017;53:5875–82.

[25] Shi Y, Lu Y, Cai Y, He Y, Zhou Y, Fang J. Evolution of particulate matter deposited in the DPF channel during low-temperature regeneration by non-thermal plasma. Fuel 2022;318:123552.

[26] Yen M, Magi V, Abraham J. Modeling the effects of hydrogen and nitrogen addition on soot formation in laminar ethylene jet diffusion flames. Chem Eng Sci 2019;196:116–29.

[27] Tang Y, Yao Q, Cui W, Zhuo J, Li S. Premixed Flame Response to a Counterflowing Non-thermal Plasma Jet. Combust Sci Technol 2019;192:2280–96.

[28] Chen Y, He LM, Fei L, Deng J, Lei JP, Yu H. Experimental study of dielectric barrier discharge plasma-assisted combustion in an aero-engine combustor. Aerosp Sci Technol 2020;99:105765.

[29] Ying Y, Liu D. Effects of butanol isomers additions on soot nanostructure and reactivity in normal and inverse ethylene diffusion flames. Fuel 2017;205:109–29.

[30] Ying Y, Xu C, Liu D, Jiang B, Wang P, Wang W. Nanostructure and oxidation reactivity of nascent soot particles in ethylene/pentanol flames. Energies 2017;10:4–6.

[31] Chen M, Liu D, Jiang B. Soot formation and combustion characteristics in confined mesoscale combustors under conventional and oxy-combustion conditions (O_2/N_2 and O_2/CO_2). Fuel 2020;264:116808.

[32] Kim S, Han K, Baek S. Influence of DC Electric Field on the Propane-Air Diffusion Flames and NO_x Formation. Energies 2021;14:1–12.

[33] Sunderland PB, Haylett JE, Urban DL, Nayagam V. Lengths of laminar jet diffusion flames under elevated gravity. Combust Flame 2008;152:60–8.

[34] Eliasson B, Kogelschatz U. Nonequilibrium Volume Plasma Chemical Processing. IEEE Trans Plasma Sci 1991;19:1063–77.

[35] Kailasanathan RKA, Zhang J, Fang T, Roberts WL. Effects of diluents on soot surface temperature and volume fraction in diluted ethylene diffusion flames at pressure. Combust Sci Technol 2014;186:815–28.

[36] Zhang Y, Liu F, Lou C. Experimental and numerical investigations of soot formation in laminar coflow ethylene flames burning in O_2/N_2 and O_2/CO_2 Atmospheres at different O_2 mole fractions. Energy and Fuels 2018;32:6252–63.

[37] Li L, Duan L, Yang Z, Zhao C. Pressurized oxy-fuel combustion characteristics of single coal particle in a visualized fluidized bed combustor. Combust Flame 2020;211:218–28.

[38] Yi W, Liu H, Feng L, Wang Y, Cui Y, Liu W, et al. Multiple optical diagnostics on effects of fuel properties on spray flames under oxygen-enriched conditions. Fuel 2021;291:120129.

[39] Zhang J, Jing W, Roberts WL, Fang T. Soot temperature and *KL* factor for

biodiesel and diesel spray combustion in a constant volume combustion chamber. Appl Energy 2013;107:52–65.

[40] Chen H, Su X, He J, Zhang P, Xu H, Zhou C. Investigation on combustion characteristics of cyclopentanol/diesel fuel blends in an optical engine. Renew Energy 2021;167:811–29.

[41] Jing W, Wu Z, Zhang W, Fang T. Measurements of soot temperature and KL factor for spray combustion of biomass derived renewable fuels. Energy 2015;91:758–71.

[42] Sayed-Kassem A, Elorf A, Gillon P, Idir M, Sarh B, Gilard V. Numerical modelling to study the effect of DC electric field on a laminar ethylene diffusion flame. Int Commun Heat Mass Transf 2021;122:105167.

[43] Song CL, Bin F, Tao ZM, Li FC, Huang QF. Simultaneous removals of NO_x, HC and PM from diesel exhaust emissions by dielectric barrier discharges. J Hazard Mater 2009;166:523–30.

[44] Davis J, Molnar E, Novosselov I. Nanostructure transition of young soot aggregates to mature soot aggregates in diluted diffusion flames. Carbon 2020;159:255–65.

[45] Reilly PTA, Gieray RA, Whitten WB, Ramsey JM. Direct observation of the evolution of the soot carbonization process in an acetylene diffusion flame via real-time aerosol mass spectrometry. Combust Flame 2000;122:90–104.

[46] Wang Y, Chung SH. Soot formation in laminar counterflow flames. Prog Energy Combust Sci 2019;74:152–238.

[47] Raj A, Yang SY, Cha D, Tayouo R, Chung SH. Structural effects on the oxidation of soot particles by O_2: Experimental and theoretical study. Combust Flame 2013;160:1812–26.

[48] Sadezky A, Muckenhuber H, Grothe H, Niessner R, Pöschl U. Raman microspectroscopy of soot and related carbonaceous materials: Spectral analysis and structural information. Carbon 2005;43:1731–42.

[49] Gaddam CK, Vander Wal RL, Chen X, Yezerets A, Kamasamudram K. Reconciliation of carbon oxidation rates and activation energies based on changing nanostructure. Carbon 2016;98:545–56.

[50] Zhang Y, Boehman AL. Oxidation behavior of soot generated from the combustion of methyl 2-butenoate in a co-flow diffusion flame. Combust Flame 2013;160:112–9.

[51] Manoj B, Kunjomana AG. Study of stacking structure of amorphous carbon by X-ray diffraction technique. Int J Electrochem Sci 2012;7:3127–34.

[52] Qi D, Yang K, Zhao X, Mei D, Ying Y. Comprehensive optical diagnostics for fl ame behavior and soot emission response to a non-equilibrium plasma. Energy 2022;255:124555.

[53] Chu H, Han W, Cao W, Gu M, Xu G. Effect of methane addition to ethylene on the morphology and size distribution of soot in a laminar co-flow diffusion flame. Energy 2019;166:392–400.

[54] Chen M, Liu D, Ying Y, Lei K, Luo M, Liu G, et al. Experimental study on soot formation, evolution and characteristics of diffusion ethylene/air flames in Ψ-

shaped mesoscale combustors. Fuel 2019;241:138–54.

[55] Liu G, Liu D, Zhu J, Wei J, Cui W, Li S. Energy conversion and ignition of fluffy graphene by flash light. Energy 2018;144:669–78.

[56] Calcote HF. Mechanisms of soot nucleation in flames—A critical review. Combust Flame 1981;42:215–42.

[57] Calotte HF. Ion and electron profiles in flames. Symp Combust 1963;9:622–37.

[58] Calcote HF, Olson DB, Keil DG. Are Ions Important in Soot Formation ? Energy and Fuels 1988;2:494–504.

[59] Place E. R. and Weinberg Felix Jiri. Electrical control of flame carbon. Proc. R. Soc. Lond. A 1966;289:192–205.